Study of the Hole Transport Processes in Solution-Processed Layers of the Wide Bandgap Semiconductor Copper(I) Thiocyanate (CuSCN)

Pichaya Pattanasattayavong, Alexander D. Mottram, Feng Yan, and Thomas D. Anthopoulos**

Wide bandgap hole-transporting semiconductor copper(I) thiocyanate (CuSCN) has recently shown promise both as a transparent p-type channel material for thin-film transistors and as a hole-transporting layer in organic light-emitting diodes and organic photovoltaics. Herein, the hole-transport properties of solution-processed CuSCN layers are investigated. Metal–insulator–semiconductor capacitors are employed to determine key material parameters including: dielectric constant [5.1 (±1.0)], flat-band voltage [–0.7 (±0.1) V], and unintentional hole doping concentration [7.2 (±1.4) × 10^{17} cm^{-3}]. The density of localized hole states in the mobility gap is analyzed using electrical field-effect measurements; the distribution can be approximated invoking an exponential function with a characteristic energy of 42.4 (±0.1) meV. Further investigation using temperature-dependent mobility measurements in the range 78–318 K reveals the existence of three transport regimes. The first two regimes observed at high (303–228 K) and intermediate (228–123 K) temperatures are described with multiple trapping and release and variable range hopping processes, respectively. The third regime observed at low temperatures (123–78 K) exhibits weak temperature dependence and is attributed to a field-assisted hopping process. The transitions between the mechanisms are discussed based on the temperature dependence of the transport energy.

1. Introduction

Belonging to the family of metal pseudohalides, copper(I) thiocyanate (CuSCN, **Figure 1**a), is one of a handful of inorganic compound semiconductors known to date to combine exceptionally high optical transparency and good hole-transporting properties.[1] Such characteristics are in great demand for a wide range of opto/electronic applications, such as the transparent charge-transporting layers in organic photovoltaics (OPVs)[2–4] and organic light-emitting diodes (OLEDs),[5,6] as well as the active channel materials in transparent thin-film transistors (TFTs) and circuits.[7,8] For the latter, the rapidly advancing development of electron-transporting (n-type) oxides, particularly amorphous indium–gallium–zinc–oxide (a-IGZO),[9] has already led to the commercialization of oxide-based TFT backplanes for flat-panel displays. The missing key ingredient for further development of next-generation transparent electronics is their hole-transporting (p-type) counterparts with comparable characteristics, since the latter would enable the development of the much desired complementary metal–oxide–semiconductor (CMOS) circuit architectures. To date, only CuSCN along with Cu_2O and SnO_x have been shown to successfully produce p-channel TFTs.[7,10] In addition to electrical performance, processing versatility is also an important consideration for manufacturing scaling-up of these future electronics in a cost-efficient manner. To this end, recent effort has been focused at developing solution-processing methods to enable the deposition of semiconducting films at low cost and onto large substrates.[7] In this respect, CuSCN can be solution-processed,[11–13] and its applications in various opto/electronic devices grown from solution have been demonstrated.[1,3–5,8,14–19] Despite the tremendous promise, however, basic understanding of the electronic properties of CuSCN is still lacking. Understanding these fundamental processes is important and could lead to the development of improved processing protocols as well as to the synthesis of new compounds with enhanced electronic properties.

Here, we report on the electronic properties, density of localized states in the mobility gap, and hole-transport mechanisms in solution-processed layers of CuSCN. Metal–insulator–semiconductor (MIS) capacitors were first developed to determine important electronic properties of CuSCN layers such as the dielectric constant (ε_s), flat-band voltage, (V_{FB}), and unintentional doping concentration (N_A), whilst TFT structures were used to

---

Dr. P. Pattanasattayavong, A. D. Mottram,
Prof. T. D. Anthopoulos
Centre for Plastic Electronics
and Department of Physics
Blackett Laboratory
Imperial College London
London SW7 2AZ, UK
E-mail: pichaya.p@vistec.ac.th; t.anthopoulos@ic.ac.uk

Dr. P. Pattanasattayavong
Department of Materials Science and Engineering
School of Molecular Science and Engineering
Vidyasirimedhi Institute of Science and Technology
Wangchan, Rayong 21210, Thailand

Prof. F. Yan
Department of Applied Physics and Materials Research Centre
The Hong Kong Polytechnic University
Hong Kong, China

DOI: 10.1002/adfm.201502953

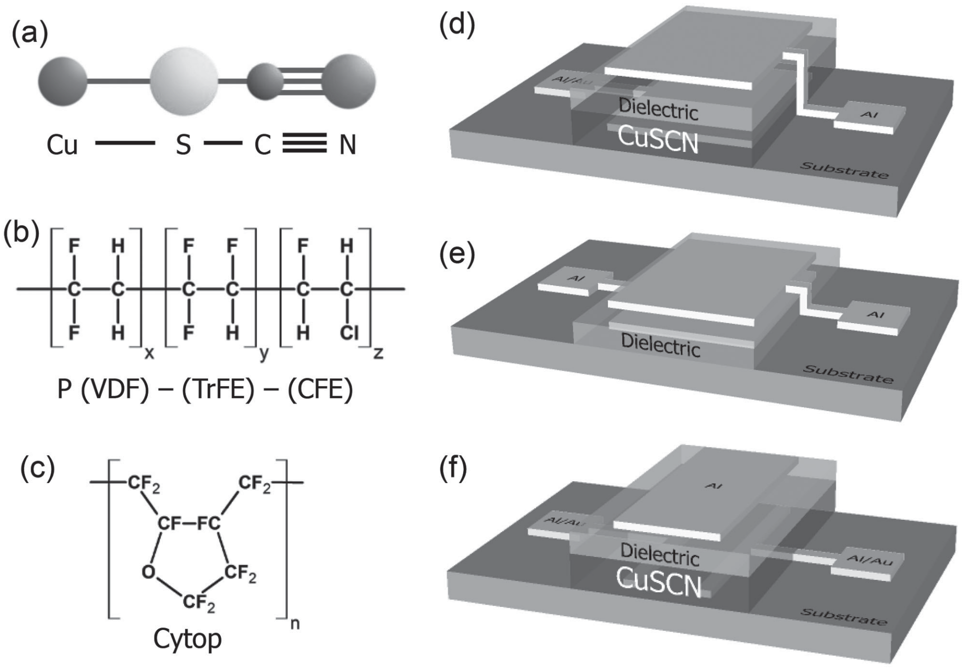

Figure 1. Schematic diagrams showing the molecular structures of a) CuSCN, b) P(VDF-TrFE-CFE), and c) CYTOP. Schematic device structures of d) MIS capacitor, e) MIM capacitor, and f) top-gate bottom-contact thin-film transistor.

determine the density of states (DOS) in the mobility gap and the hole-transport processes governing transistor operation. The method employed for the calculation of the localized DOS follows the procedure of Grünewald and Thomas, which allows the extraction of DOS from a single transfer curve[20] while the analysis of the evolution of the field-effect mobility (μ_{FE}) with temperature allows the study of hole-transport mechanism. Since the transport characteristics of TFTs can be affected by the nature of the material used as the gate insulator, top-gate bottom-contact (TG-BC) CuSCN transistors with two different polymeric dielectrics, namely the high-*k* relaxor ferroelectric poly(vinylidene fluoride-trifluoroethylene-chlorofluoroethylene) [P(VDF-TrFE-CFE), Figure 1b] and the fluoropolymer CYTOP (Figure 1c), were analyzed and compared to ensure that the obtained results represent the intrinsic properties of CuSCN and not affected by the choice of the dielectric. The temperature dependences of the dielectric properties of both gate insulators were also studied in order to account for their influence on the transistor characteristics as a function of temperature.

2. Experiments and Methods

Three different device structures were developed and studied. The first structure, the MIS capacitor (Figure 1d), was used in capacitance–voltage (*C–V*) measurements for calculating the ε_s, V_{FB}, and N_{A} of CuSCN. The metal–insulator–metal MIM structure (Figure 1e) was used for the geometric capacitance estimation of P(VDF-TrFE-CFE) and CYTOP layers. The temperature-dependent geometric capacitances calculated from the MIM capacitors were subsequently used for the estimation of the hole field-effect mobility in CuSCN layers. Finally, the TG-BC transistors (Figure 1f) based on CuSCN and the two polymeric dielectrics were employed to study the localized states DOS and hole-transport mechanisms within the CuSCN channel. The comparative use of two different dielectrics helped to identify whether the temperature-dependent behavior observed is a result of the dielectric(s)/semiconductor interface or the semiconductor itself.

2.1. Sample Preparations and Measurements

2.1.1. Capacitance–Voltage Measurements

MIS capacitors using P(VDF-TrFE-CFE) as the insulator and CuSCN as the semiconductor (Figure 1d) were fabricated as follows. Al/Au (5/25 nm) contacts were deposited onto glass substrates by thermal evaporation through shadow masks. The thin Al layer was used to improve adhesion between the injecting Au contacts and the glass substrates. CuSCN was spin-cast from a saturated solution in dipropyl sulfide onto the Au contacts, followed by drying at 80 °C for 15 min. The process yields CuSCN thin films of 17.5 (±2.5) nm thick as measured by the Dektak profilometer and verified by optical reflectometry. Details of solution preparation and spin-casting parameters can be found elsewhere.[8] As-prepared films are nanocrystalline as seen in the atomic force microscopy images displayed in **Figure 2** in agreement with previous reports.[8] Analysis of film's surface yields a root mean square (r.m.s.) value for the surface roughness of 1.73 nm—a relatively low value indicative of the rather smooth film surface. The dielectric P(VDF-TrFE-CFE) with composition of 56/36.5/7.5 mol%, synthesized via the suspension polymerization process,[21,22] was spin-cast from a 30 mg mL^{-1} solution in 2-butanone and annealed at 60 °C for 3 h. The dielectric thickness was 220 (±5) nm also measured

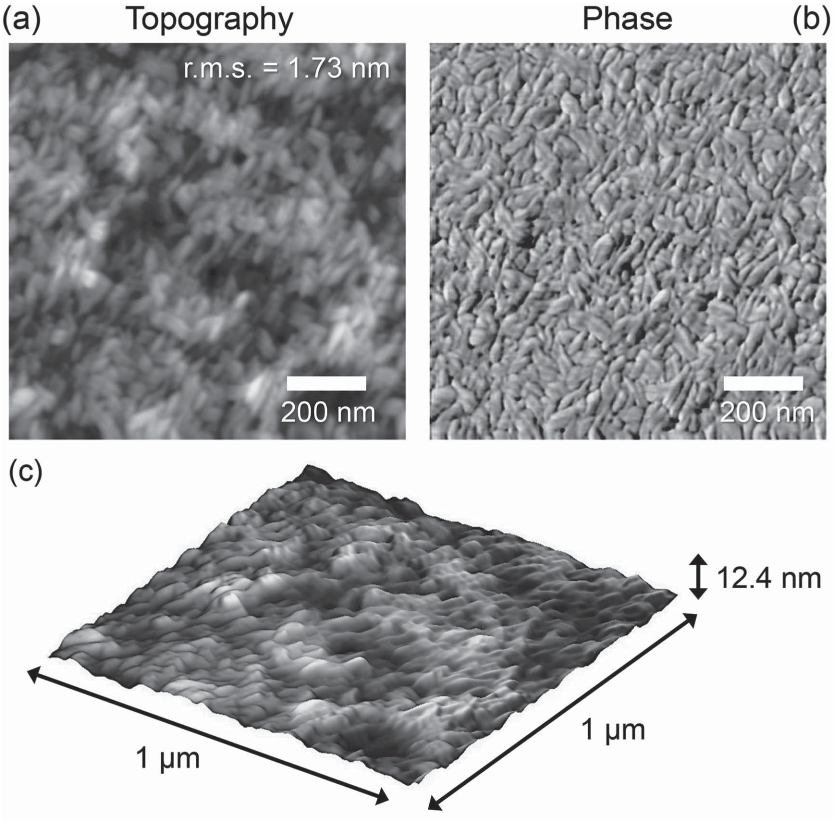

Figure 2. Surface analysis of solution-processed CuSCN layers by atomic force microscopy. a) Surface topography and b) phase images of a representative CuSCN layer employed in this study. c) 3D representation of the surface topography AFM image in (a). The root mean squared (rms) surface roughness value extracted from (a) is 1.73 nm.

by the profilometer. Al (40 nm) contacts were then deposited onto the dielectric by thermal evaporation through shadow masks. All fabrication steps were conducted in nitrogen atmosphere, and the resulting stack of Au/P(VDF-TrFE-CFE)/CuSCN formed the MIS capacitor. The same deposition sequence was also used for the fabrication of CuSCN TG-BC transistors as described below.

The C–V characteristics of two 4 mm^2 and two 8 mm^2 MIS capacitors were measured using a Solartron 1260 impedance analyzer with the samples mounted in a Janis ST-500 probe station. The measurement was carried out under high vacuum (10^{-5} mbar) at room temperature (≈293 K). The large width-to-thickness ratio of the capacitors ensured that effects of fringing electric field were negligible. The geometric capacitance (capacitance per unit area in F cm^{-2}) averaged from these four capacitors was used for the calculations of ε_s, V_{FB}, and N_A.

2.1.2. Temperature Dependence of Dielectric Properties

Simple MIM capacitors employing either P(VDF-TrFE-CFE) or CYTOP (Asahi Glass) as the insulator and Al contacts (Figure 1e) were fabricated on glass substrates. First, bottom Al contacts were thermally evaporated through shadow masks followed by the spin-casting of the dielectric layer. The processing steps of P(VDF-TrFE-CFE) were the same as described in the previous section whereas CYTOP was spin-cast at 2000 rpm for 60 s and annealed at 100 °C for 30 min in nitrogen atmosphere. Finally, the top Al contacts were also deposited by thermal evaporation through shadow masks.

The impedance of the MIM capacitors was measured using the Solartron 1260 impedance analyzer. The samples were placed in a Janis ST-500 cryogenic probe station under high vacuum of 10^{-5} mbar, and cooled down to 77 K using liquid nitrogen. The temperature was controlled by a Scientific Instruments 9700 temperature controller which continuously adjusted the heating. Low outgassing, thermally conductive, electrically insulating vacuum grease was used to mount the samples to insure that they were at thermal equilibrium with the sample holder. Four CYTOP capacitors and four P(VDF-TrFE-CFE) capacitors with areas ranging between 6 and 16 mm^2 were measured at different temperatures in the range 78–318 K. The average temperature-dependent geometric capacitances were used in the subsequent analysis.

2.1.3. Temperature Dependence of Field-Effect Hole-Transport

TG-BC transistors employing CuSCN as the semiconductor and either CYTOP or P(VDF-TrFE-CFE) as the dielectric were fabricated on glass substrates (Figure 1f). The ordering of the layers as well as the processing sequence were the same as those of the MIS capacitors previously described, with an exception that a different set of shadow masks was used to define source/drain/gate (S/D/G) electrodes. From the bottom to the top, the structure consisted of thermally evaporated Al/Au S/D contacts, spin-cast CuSCN, spin-cast dielectric [either CYTOP or P(VDF-TrFE-CFE)], and thermally evaporated Al gate electrodes.

Current–voltage (I–V) characteristics of the transistors were measured with a Keithley 4200 semiconductor parameter analyzer. Similar to the measurements of the MIM capacitors, the samples were placed inside the vacuum cryogenic probe station, and the measurements were conducted in the temperature range 78–318 K. Four transistors based on CuSCN/CYTOP and four based on CuSCN/P(VDF-TrFE-CFE) with channel width (W) of 1500 µm and channel lengths (L) of 30 µm and 40 µm (two of each length for each CuSCN/dielectric set) were measured. The transfer characteristics of the CuSCN TFTs measured at room temperature were found to be stable when stored under inert atmosphere for several months and consistent with previously published data.[1,8] All transistors measurements were performed either in nitrogen atmosphere or in high vacuum (10^{-5} mbar) in order to avoid unintentional p-doping effect. The latter has been shown to greatly impact the electronic properties of CuSCN layers and the operating characteristics of the resulting transistors.[1]

2.2. Parameters Extraction

2.2.1. Dielectric Constant, Doping Concentration, and Flat Band Voltage Analysis

A number of important parameters were determined from the MIS capacitor measurements, including the dielectric constant of the semiconductor ε_s, the doping concentration N_A (where the subscript A signifies that the dopants are of the acceptor type), and flat-band voltage (V_{FB}). Following the standard MIS theory,[23,24] the total capacitance of the MIS structure C_{MIS} is a series combination of the insulator capacitance C_i and the semiconductor capacitance C_s given as

$$\frac{1}{C_{MIS}} = \frac{1}{C_i} + \frac{1}{C_s} \tag{1}$$

In full accumulation all the voltage in a MIS capacitor drops across the insulator and therefore the total accumulation capacitance ($C_{MIS,acc}$) is equal to the capacitance of the insulator ($C_{MIS,acc} = C_i$). On the other hand, when fully depleted C_s can be determined once the depletion capacitance $C_{MIS,dep}$ and C_i are known. The dielectric constant ε can then be calculated using

$$C = \frac{\varepsilon\varepsilon_0}{d} \tag{2}$$

where ε_0 is the vacuum permittivity and d is the layer thickness. In the case of a spatially uniform doping concentration profile, N_A can be determined using[23,24]

$$N_A = \frac{2}{q\varepsilon_s\varepsilon_0}\left|\frac{d}{dV}\left(\frac{1}{C_{MIS}^2}\right)\right|^{-1} \tag{3}$$

where q is the elementary charge and V is the voltage. Graphically, N_A can be calculated by plotting $1/C_{MIS}^2$ versus V and taking the slope of the linear part of the plot before multiplying its inverse with $2/q\varepsilon_s\varepsilon_0$. The flat band voltage V_{FB} may also be directly estimated from the x-intercept of this plot. Alternatively, V_{FB} can also be taken from the measured C–V characteristics as the voltage at which the semiconductor flat band capacitance $C_{s,FB}$ occurs. The latter is determined from

$$C_{s,FB} = \frac{\varepsilon_s\varepsilon_0}{L_D} \tag{4}$$

where L_D is the Debye length

$$L_D = \sqrt{\frac{\varepsilon_s\varepsilon_0 kT}{q^2 N_A}} \tag{5}$$

In Equation (5) k is the Boltzmann constant and T the temperature. By substituting C_s in Equation (1) with $C_{s,FB}$, we can obtain the total MIS capacitance at flat band $C_{MIS,FB}$. It then follows that V_{FB} is the voltage at which the capacitance is equal to $C_{MIS,FB}$.

2.2.2. Extracting the Density of Localized States

As mentioned in Section 1, the extraction of the DOS will follow the method developed by Grünewald et al.[20] It should be noted that other methods which are similarly based on the analysis of one of the transistor characteristics also exist but they are generally suitable for a semiconductor that shows only one type of temperature dependence. As will be shown later, the case of CuSCN studied here appears to feature three different transport regimes with three different temperature dependencies which do not permit a straightforward use of these methods. Kalb and Batlogg have reviewed a number of different methods and found that the Grünewald procedure yields reasonably good results.[25] The procedure relies on a convolution of the DOS and the Fermi function to find the charge carrier density

$$p = \int g(E)[1 - f(E)]\,dE \tag{6}$$

where p is the hole density, $g(E)$ is the hole DOS, and $f(E)$ is the Fermi–Dirac distribution. If p is known, then $g(E)$ can be found by deconvoluting Equation (6). Based on the Grünewald method,[20,25] p can be expressed in terms of the surface potential V_0 at the semiconductor/dielectric interface as

$$p(V_0) = \frac{C_i^2}{q\varepsilon_s\varepsilon_0}\tilde{V}_G\left(\frac{dV_0}{d\tilde{V}_G}\right)^{-1} \tag{7}$$

where $\tilde{V}_G$ is V_G–V_{FB}, and V_0 can be obtained by numerically solving the equation

$$\exp\left(\frac{qV_0}{kT}\right) - \frac{qV_0}{kT} - 1 = \frac{qC_i d_s}{kT\varepsilon_s\varepsilon_0 I_0}\left[I_D\left(\tilde{V}_G\right)\tilde{V}_G - \int I_D\left(\tilde{V}_G\right)d\tilde{V}_G\right] \tag{8}$$

where d_s is the semiconductor thickness and I_0 is the background off current of the semiconductor. By using the zero-temperature approximation,[25] g can be expressed in terms of $\tilde{E} = qV_0$ as

$$g(\tilde{E}) \approx \frac{1}{q}\frac{d}{dV_0}\left[p(V_0)\right] \tag{9}$$

Using the transistor transfer characteristics measured in the linear regime, we can obtain V_0 as a function of $\overline{V}_G$ by solving Equation (8). Then, $p(V_0)$ and $g(\overline{E})$ can be found from Equations (7) and (9), respectively. Note that $g(\overline{E})$ in this case is a function of the energy relative to the Fermi level (E_F). If the latter is known, then the DOS can be placed in the semiconductor energy diagram by shifting the energy scale from ($\overline{E}$) to $E = E_F - \overline{E}$ (where we use the valence mobility edge as the origin, $E_V = 0$, and energies above it are defined as positive).

Qualitatively, the basics of the Grünewald method may be explained as follows. The application of the gate voltage V_G causes the band-bending in the semiconductor, and the potential V_0 is the resulting potential at the semiconductor/dielectric interface.

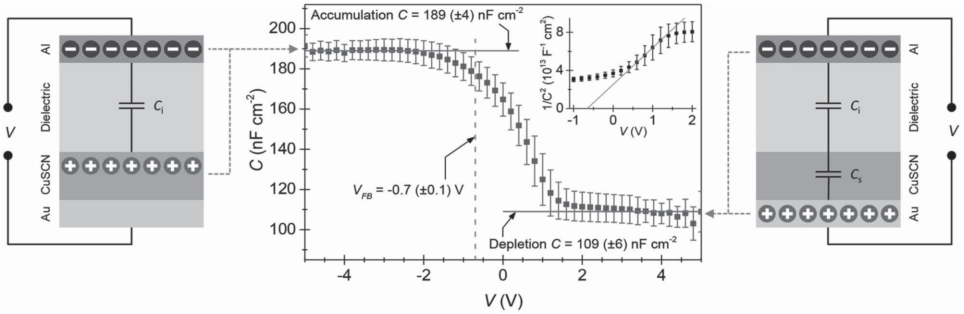

Figure 3. C–V plot of the CuSCN/P(VDF-TrFE-CFE)/Al MIS capacitors. Data points are the average geometric values from four MIS capacitors with areas of 4 or 8 mm^2. Error bars show the standard deviation of each point. The inset shows the plot of $1/C^2$ versus V and the linear fit (solid line) used for the calculation of doping concentration N_A and flat band voltage V_{FB}. The two schematics on the left and right show the MIS capacitor under accumulation and depletion regimes, respectively.

The band-bending also results in a change in the occupancy of the DOS as the energy difference between E_F and the mobility edge (E_V in the case of CuSCN) changes. For the accumulation mode, more band-bending (increasing V_0) causes E_V to move closer to E_F (or equivalently the movement of E_F toward E_V because the carrier density is in fact determined by the relative position between E_F and E_V). Since the occupancy is known (Fermi–Dirac statistics), tracing the carrier density as E_F moves toward E_V (by the Grunewald method) allows the determination of the DOS.

2.2.3. Field-Effect Hole Mobility in CuSCN Layers

The investigation of charge transport in field-effect transistors is generally based on the temperature dependence of the charge carrier mobility (μ). To ensure that the conducting channel under investigation is uniform, only the linear mobility (μ_{lin}) is used. This is extracted from a transfer plot of a transistor operating in the linear regime (small drain voltages V_D), according to

$$\mu_{\text{lin}} = \frac{1}{C_i V_D} \frac{L}{W} \frac{\partial I_{D,\text{lin}}}{\partial V_G} \tag{10}$$

where $I_{D,\text{lin}}$ is the drain current measured as a function of the gate voltage (V_G) in the linear regime, and L/W are the channel length/width, respectively. Another important parameter is the threshold voltage (V_{TH}), which can be obtained from the x-intercept of the plot of $\sqrt{I_{D,\text{sat}}}$ versus V_G. Note that in the latter case the channel current is measured in saturation ($V_D \geq V_G - V_{TH}$).

3. Results and Discussion

3.1. Metal–Insulator–Semiconductor Capacitors Based on CuSCN

The C–V characteristics (10 Hz) of the Au/P(VDF-TrFE-CFE)/CuSCN MIS capacitors is plotted in **Figure 3**. All four MIS capacitors showed typical hole-accumulation behavior, evolving from depletion to accumulation with decreasing gate voltage. No inversion regime could be observed even at low measuring frequencies. The latter observation implies that the Fermi energy E_F lies significantly away from the intrinsic Fermi energy level (E_i) located at the mid gap, confirming the dominant p-type characteristics of the solution-processed CuSCN layers. To this end, we have earlier reported the ultraviolet photoelectron spectroscopy (UPS) measurements which showed that the E_F was 0.63 eV above the valence mobility edge of CuSCN films drop-cast onto Au.[1] However, we do stress that the E_F in the MIS and transistor structures based on spin-cast CuSCN used here may differ due to the structural, morphological, or interfacial variations.

The accumulation capacitance, which corresponds directly to the capacitance of the insulator, is measured to be 189 (±4) nF cm^{-2}. The high capacitance is expected due to the use of the high-k relaxor ferroelectric terpolymer P(VDF-TrFE-CFE). From the measured thickness of 220 (±5) nm, the dielectric constant of the polymer is calculated from Equation (2) as 47 (±2). In the depletion regime, the average capacitance of the MIS structure is 109 (±6) nF cm^{-2}, yielding a CuSCN layer capacitance of 258 (±34) nF cm^{-2} [Equation (1)]. The dielectric constant of CuSCN, ε_s, is computed from Equation (2) using the measured thickness of 17.5 (±2.5) nm and found to be 5.1 (±1.0). An earlier ellipsometry measurement on CuSCN film found that the dielectric constant in the optical frequency range (10^{14}–10^{15} Hz) was 3.5.[1] The higher value obtained in this work from a lower excitation frequency is therefore logical because more polarization mechanisms become active at lower frequencies, contributing to a higher dielectric constant value. The ε_s value obtained here will be regarded as a quasistatic dielectric constant of CuSCN and used in the subsequent calculations. As a reference, ε_s of common semiconductors for organic and oxide electronics are also given here. The ε_s values of inorganic semiconductors ZnO, In_2O_3, and SnO_2 are 8.5, 8.9, and 9.7, respectively,[26–28] while those for the organic semiconductors rubrene, pentacene, and poly(3-hyxylthiophene) (P3HT) are 3.3–3.9, 2.6, and 4.4, respectively.[29–31] The derived value of ≈5 lies between the two groups and possibly reflects the weaker ionic or stronger covalent character of CuSCN due to the –SCN constituent.

The plot of $1/C^2$ versus V (inset in Figure 3) allows the estimation of doping concentration N_A and the flat band voltage V_{FB}. A linear fit to this plot (line) over the range which C changes suggests a uniform doping concentration from which N_A can be calculated using Equation (3). The spatially

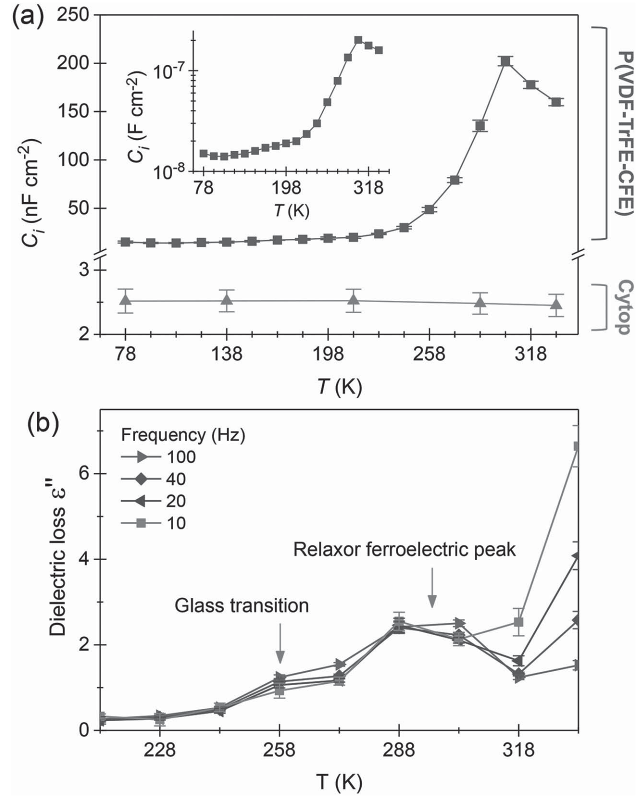

Figure 4. a) Temperature dependence of the geometric capacitance (C_i) of the two dielectric polymers used, each averaged over four MIM capacitors fabricated simultaneously. The inset shows the results of P(VDF-TrFE-CFE) on a semi-log scale. b) Temperature dependence of the dielectric loss (ε'') of P(VDF-TrFE-CFE) showing the peaks corresponding to the glass transition and the relaxor ferroelectric relaxation temperatures.

uniform doping profile assumption is expected to hold reasonably well in this case since these dopants are unintentionally incorporated species, which could be structural defects, crystallographic defects, or chemical impurities. Because the film was prepared from a single casting step in nitrogen atmosphere, any unintentional dopants should be uniformly distributed within the film. Based on this assumption, N_A is found to be 7.2 (±1.4) × 10^{17} cm^{-3}. Using the crystallographic data of CuSCN,[32–34] the number densities of CuSCN units are in the range of (1.4–1.5) × 10^{22} cm^{-3}. The doping density is therefore approximately 50 parts per one million CuSCN units (≈50 ppm). Finally, the value of $C_{MIS,FB}$ is calculated to be 167 (±6) nF cm^{-2}, which yields a possible range for V_{FB} between 0 and −0.85 V. Indeed, the intercept of the $1/C^2$ versus V plot yields a V_{FB} value of −0.7 (±0.1) V.

3.2. Temperature Dependence of the Dielectric Properties

Since P(VDF-TrFE-CFE) is known to show a strong temperature dependence,[35–37] it is imperative to understand its thermal response to allow a comprehensive analysis of the transistor using this material as a dielectric. The average geometric capacitance (C_i) of P(VDF-TrFE-CFE) MIM capacitors measured at 10 Hz is shown in **Figure 4**a. The extracted value ranges between 14 and 15 nF cm^{-2} in the low temperature range of 78–138 K, before rising rapidly and peaking at 202 (±5) nF cm^{-2} at 303 K. This peak is a well-documented characteristic of P(VDF-TrFE-CFE) and is a result of its relaxor ferroelectric behavior.[35–37] The measured geometric capacitance at each temperature will be used for the subsequent calculations of hole mobility in CuSCN transistors. Figure 4b shows the temperature dependence of the dielectric loss of P(VDF-TrFE-CFE). Apart from the relaxor ferroelectric peak already mentioned, a smaller peak at 258 K is attributed to the glass transition (T_g) of the polymer,[36,37] and this temperature also coincides with the peak in the hole mobility of P(VDF-TrFE-CFE)-based transistors as will be shown later. In addition, the temperature dependence of the amorphous fluoropolymer CYTOP is also shown in Figure 4a. The geometric capacitance of CYTOP is found to be independent of the temperature with a value of 2.5 (±0.2) nF cm^{-2} throughout the measured temperature range. This is not surprising since the T_g of CYTOP, according to the product details from Asahi Glass, is ≈381 K, i.e., a temperature well outside the temperature range investigated here.

3.3. Density of States in Spin-Cast Layers of CuSCN

The hole density of states (DOS) provides the foundation on which carrier transport theory can be built. First, an analysis of the transistor transfer characteristics measured at 288 K using the Grünewald method was performed. It is important to note that the method requires the measurement of the off channel current [I_0 in Equation (8)], which serves as the starting reference point for the determination of the DOS. The accurate measurement of I_0 can be affected by both the experimental noise and the gate leakage current, the latter of which can be relatively high in transistors based on thin polymer dielectrics. Another feature that may affect the measured I_0 is the leakage current from interface trap states that could possibly form a percolation pathway between the source and the drain contacts. The combined leakage current can mask the true off current flowing in the semiconductor, affecting the lower bound of the DOS calculation.

Figure 5a shows the results from the localized states DOS extraction by the Grünewald method. The open symbols, denoting the DOS obtained from all four CYTOP-based transistors, appear to well represent an exponential tail. The DOS covers at least 0.35 eV of the energy range and extends over 10^{17} to 10^{21} cm^{-3} eV^{-1}. The results from the P(VDF-TrFE-CFE)-based devices are shown as half-filled symbols and, at first, appear to display an increase of at least two orders of magnitude when compared to the DOS from the CYTOP-based devices as well as the presence of the rapidly increasing DOS beyond 0.25 eV. However, as noted above, the lower bound of the DOS extraction can be affected by the level of I_0, and could be significant in the case of the thinner P(VDF-TrFE-CFE) layers. The thickness of CYTOP was measured as ≈900 nm while that of the high-k polymer was only ≈220 nm. Indeed, the former dielectric led to a value of $I_0 \approx 10^{-12}$ A, while the latter to $I_0 \approx 10^{-9}$ A. Assuming that the value for I_0 of CYTOP is a better estimation of the true off-current in the semiconductor, the DOS of

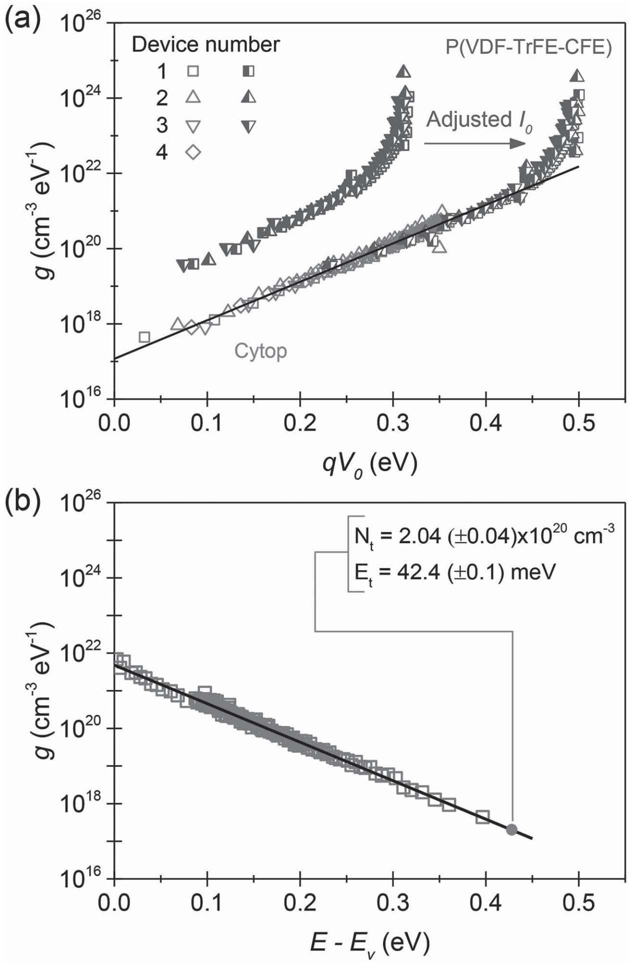

Figure 5. a) Density of localized states for CuSCN extracted from field-effect transistor measurements using the Grünewald method. Open symbols are from CYTOP-based devices while half-filled symbols are from P(VDF-TrFE-CFE)-based devices. The latter are replotted again after adjusted with the off current from the CYTOP-based devices (presumed as a better estimation for the real off current in the semiconductor). The solid line is the exponential fit to the DOS. b) Combined localized states DOS positioned relative to the hole mobility edge ($E_v = 0$). The solid line is the exponential fit.

the P(VDF-TrFE-CFE)-based transistors were then re-calculated using I_0 value from the CYTOP-based devices. The adjusted DOS, plotted again as half-filled symbols in Figure 5a, appears to be shifted along the energy axis and now shows excellent overlap and continuation with the DOS extracted from the CYTOP-based transistors. The linear regime in the semilogarithmic plot has been fitted (solid line) with an exponential function [$g \propto \exp(qV_0/E_t)$], and its characteristic energy (sometimes called the width) E_t which describes the energetic spread of the DOS is found to be 42.4 (±0.1) meV, corresponding to a characteristic temperature T_t (from $E_t = kT_t$) of 492 (±2) K.

It should also be noted that the range of qV_0 is different between CYTOP-based and P(VDF-TrFE-CFE)-based devices. The former stops at approximately 0.35 eV while the latter continue onward and extends into the region of qV_0 where the DOS increases rapidly. The values beyond ≈0.45 eV tend to unrealistic numbers for the DOS; for example, the DOS of band states calculated with the reported values of effective masses by Jaffe et al.[38] is on the order of 10^{22} cm^{-3} eV^{-1}. It may be possible that the rapidly increasing part of the DOS in the high qV_0 range is a systematic error caused by E_F reaching the extended hole states (approximately band states) resulting in a breakdown in the analysis, or more specifically the Boltzmann approximation used by Grünewald et al. is not valid when E_F is close to E_V. Based on this argument, it is assumed that the breakdown point at ≈0.45 eV is the mobility edge. This allows the DOS to be positioned in the mobility gap as shown in Figure 5b as well as fitted to the general expression of the exponential localized states DOS given by

$$g(E) = \frac{N_t}{E_t}\exp\left(-\frac{E}{E_t}\right) \tag{11}$$

The concentration of the localized states N_t is then determined to be 2.04 (±0.04) × 10^{20} cm^{-3}. Although we acknowledge the ambiguity in positioning the DOS using this method, we note that E_t is not affected by the relative position of the DOS and E_V and remains the same as determined previously, i.e., 42.4 (±0.1) meV or 492 (±2) K. As will be seen in the next section, the charge transport properties mainly depend on E_t; therefore, the uncertainty of positioning the DOS (and hence N_t) has no substantial effects on understanding the carrier transport process. For comparison, **Table 1** lists the characteristic energies and temperatures of a number of inorganic and organic semiconductors. The value of CuSCN obtained in this work falls in the same range as those from the hole-transporting inorganic systems.

Another interesting consideration is the temperature dependence of the localized states DOS. The identities of the localized states are still under debate, but generally the tail states (closer to the mobility edge) are associated with the disorder in the material while the deep states are attributed to defects and chemical impurities.[39–41] The disorder of the tail states can be

Table 1. Characteristic energy E_t and temperature T_t of the localized states distribution in various organic and inorganic semiconductors.

Semiconductor	E_t [meV]	T_t [K]	Ref.
CuSCN	42.4	492	a)
a-Si, a-Si:H (*electron*)	20–30	232–348	[39,51]b)
a-Si, a-Si:H (hole)	30–50	348–578	[54,65]b)
a-As$_2$Se$_3$ (*hole*)	50	578	[54,66]
a-IGZO (*electron*)	20	232	[51]
Pentacene	33, 40–60	385, 464–696	c,d)
PTV	33	380	d)
P3HT	27, 37	310, 425	d)
PQT-12	28	324	d)
6T	39	455	d)
DH6T	43	495	d)
PPV	47	540	d)

a)This work; b)Ref. [67] and references therein; c)Ref. [25] and references therein; d)Ref. [53] and references therein.

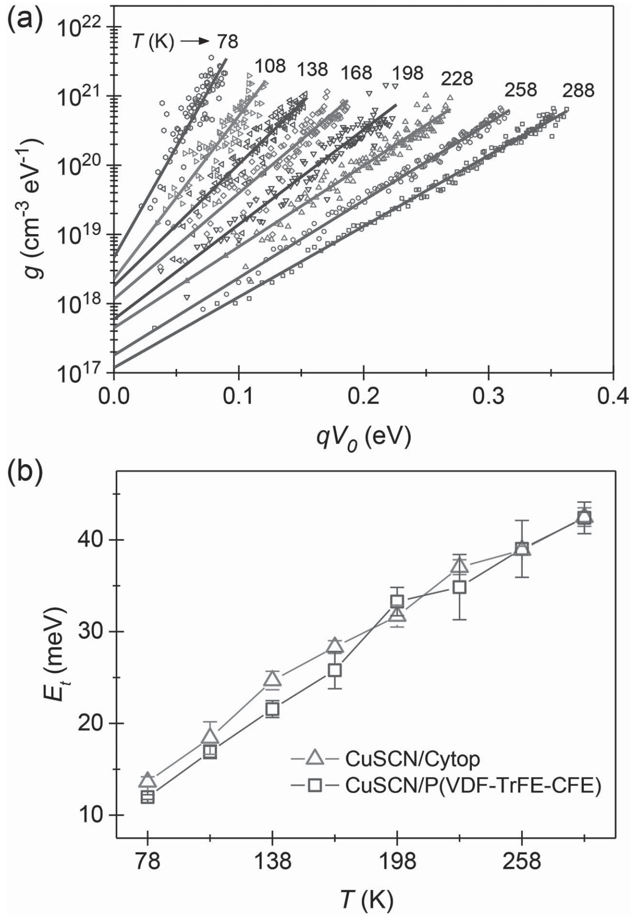

Figure 6. a) Density of localized states calculated from CuSCN field-effect transistor measurements at various temperatures. Only the data from CYTOP-based devices is shown for clarity. The solid lines are the exponential fits to the data. b) Localized states characteristic energy E_t obtained from the width of the exponential DOS as a function of temperature.

further categorized into thermal disorder, e.g., the dynamic disorder due to phonon coupling which is important in organic materials,[42,43] and structural disorder, e.g., the static disorder due to spatial variation of the lattice in amorphous semiconductors.[39,41] The localized states in inorganic semiconductors are generally attributed to the latter only and treated as temperature-independent. However, some authors have reported that the disorder in such materials can in fact be a combination of both thermal and structural disorder, and hence also dependent on the temperature.[44–46] Indeed by analyzing our data from 288 down to 78 K in steps of 30 K, systematic shift in the DOS can be observed as shown in **Figure 6**a. The DOS characteristic energy is also found to monotonically decrease with the decreasing temperature as plotted in Figure 6b. Similar behavior has also been seen in the analysis of the optical absorption coefficient of a-Si:H by Cody et al.[45] and clarified further by Aljishi et al.[46] using photoelectron spectroscopy. Both reports also show the "freeze-in" of the localized states, which is the leveling off of E_t to a constant value below a certain temperature. This feature is absent in our case, which could possibly imply that the freeze-in temperature of CuSCN was not reached. However, it is noted that further evidence is still needed to verify that the temperature dependence of the localized states in CuSCN seen here is not a result of systematic errors inherent in the DOS calculation method.

3.4. Hole Transport in Solution-Processed CuSCN Layers

Typically the analysis of charge transport properties from transistor characteristics is based on the plot of $\ln(\mu)$ versus T at a constant V_G. This is because the semiconducting channel conditions (e.g., charge density) are usually assumed to be the same for each V_G. Each curve then carries the information regarding the charge transport under one circumstance. However, in our case the operating voltage range of CuSCN transistors based on two different dielectrics, CYTOP and P(VDF-TrFE-CFE), differ significantly due to their different geometric capacitances and the temperature dependence of P(VDF-TrFE-CFE). In order to ensure that we analyze and compare the results under similar channel conditions, we use the plot of $\ln(\mu)$ versus T for each gate-induced carrier concentration N_G, which can be calculated from $N_G = C_i\,(V_G - V_{TH})$. The threshold voltage (V_{TH}) is also included in order to compensate for the difference in the turn-on voltage V_{ON} of the two sets of transistors. While obtaining V_{ON} from the transistor characteristics can be ambiguous, we use V_{TH} obtained from the standard procedure following the gradual channel approximation as described previously.

The results for $N_G = 1 \times 10^{11}$, 5×10^{11}, and 1×10^{12} cm^{-2} are shown in **Figure 7**. The data from CuSCN transistors based on CYTOP dielectric are plotted as solid symbols whereas those based on P(VDF-TrFE-CFE) dielectric are open symbols. The two sets of data show very similar behavior, assuring that the temperature evolution seen here is characteristic of CuSCN. The temperature dependence of the hole mobility shown in Figure 7 displays three main transport regimes: (1) from 303 down to 228 K where μ_{lin} is thermally activated with a large activation energy; (2) between 228 and 123 K where μ_{lin} is also thermally activated but with a smaller activation energy; and (3) below 123 K where μ_{lin} shows only slight dependence on temperature. These three temperature regimes suggest different charge carrier transport mechanisms. Similar behavior has also been observed, for example, in amorphous silicon (a-Si) and polycrystalline organic semiconductors.[40,47–49] Additionally, there is also the high temperature regime where μ_{lin} decreases, which may be due to thermal changes in the semiconductor[50] and possibly also in the dielectrics as well.

Typically, the discussion about carrier transport in non-crystalline inorganic semiconductors (the morphology of our CuSCN film is nanocrystalline as previously reported[1,8] and clearly seen in the AFM images of Figure 2) centers around the multiple trapping and release (MTR) model.[39–41,51,52] According to this theory, carriers residing in the localized states are immobile, and only those in the extended states can transport the charges. Due to the inherent charge concentration dependence that is built-in to how field-effect mobility μ_{FE} is calculated,[53] the latter parameter depends on the ratio between the number of majority carriers thermally activated to the extended states to the number of carriers induced by the gate field and is given as[20,33]

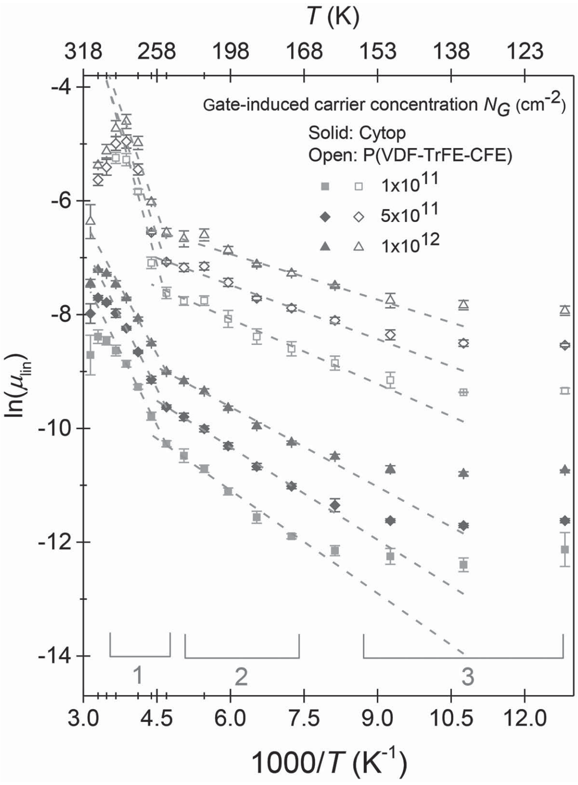

Figure 7. Evolution of field-effect hole mobility with temperature of both P(VDF-TrFE-CFE)-based (open symbols) and CYTOP-based (solid symbols) CuSCN transistors. Each color shows the results extracted from a fixed gate-induced carrier density.

$$\mu_{\mathrm{FE}} = \mu_{\mathrm{h}} \frac{p_{\mathrm{mobile}}}{p_{\mathrm{G}}} \tag{12}$$

where μ_{h} is the physical mobility of holes, p_{mobile} is the number of holes in the extended states which are mobile, and p_{G} is the number of holes induced by the gate field. It is the ratio $p_{\mathrm{mobile}}/p_{\mathrm{G}}$ that carries forward the temperature activation into the measured field-effect mobility. The final expression of Equation (12) takes the generic form of

$$\mu_{\mathrm{FE}} = \mu_0 \exp\left(\frac{E_{\mathrm{a}}}{kT}\right) \tag{13}$$

where μ_0 is the mobility prefactor, and E_{a} is the activation energy (here we have omitted the field dependence as it is beyond the scope of this work). The definition of the mobility prefactor varies depending on the details of the treatment of the MTR model but generally contains at least the physical mobility and the ratio between the effective density of the extended states and the density of the localized states.[39,41,52,53] The activation energy is associated with the energetic distance between the mobility edge and the peak of the distribution of carriers residing in the localized states.[41,52]

In some cases, the MTR model is valid down to a certain temperature below which the temperature dependence changes—the mobility still remains temperature activated, but the activation energy decreases. It has been proposed that the mode of transport changes from the MTR regime to variable range hopping (VRH) regime.[40,54,55] The temperature dependence of carrier transport in the VRH regime has its ground on the form of the localized states DOS. In other words, the energetic distribution of the localized states influences how the hopping of the carriers proceeds, and hence affects its temperature dependence. For an exponential DOS, there are more states at higher energies (i.e., more states nearer to the mobility edge), hence an upward hop in energy is more probable as the transition is weighted by both the energy of the carrier and the density of states at each energy.[56] Considering the whole DOS of the localized states, it can be shown that there is a particular energy level where the carriers hop to on average. This is where the carrier transport takes place, and such an energy level is called the transport energy E_{TR}.[54,57–60] The exact expression for E_{TR} depends on how the problem is defined mathematically but generally is of the form

$$E_{\mathrm{TR}} = kT_{\mathrm{t}} \ln\left[C \frac{\left(\gamma/N_{\mathrm{t}}^{1/3}\right)}{(T_{\mathrm{t}}/T)}\right] \tag{14}$$

where C is some constant, γ is the inverse wavefunction decay length, and N_{t} and T_{t} are the parameters of the localized states DOS defined in Equation (11). The two ratios in the logarithm correspond to the contributions from spatial and energetic domains, which are the basic of the hopping rate in the VRH theory. The spatial term $\gamma/N_{\mathrm{t}}^{1/3}$ is the ratio of the average distance between the localized states to the wavefunction decay length, and the energetic term (T_{t}/T) is the ratio of the characteristic temperature of the localized states distribution to the lattice temperature. Based on the transport energy, the carrier transport in the VRH regime can be treated similar to that in the MTR regime, but instead of the mobility edge, the transport now happens at E_{TR}. The mobility is still temperature activated and can also be described with Equation (13). The activation energy scale is now on the order of the characteristic energy of the DOS of the localized states.[60]

Due to the temperature dependence of E_{TR}, at high temperatures E_{TR} coincides and is fixed at the mobility edge, and the transport mode is MTR. With decreasing temperature, E_{TR} falls below the mobility edge, changing the transport mode to VRH.[58–60] However, due to the existence of E_{TR}, the carrier mobility is still temperature activated albeit with a different activation energy. At very low temperatures, E_{TR} approaches the thermal equilibrium Fermi level. In this last regime, Mott's model of VRH predicts a temperature dependence which varies with $\exp\left(T^{-1/4}\right)$,[61] but other models have also been proposed, such as the field-assisted hopping which leads to the temperature independence.[62–64]

Based on the exponential DOS of the localized states in CuSCN obtained in the previous section, E_{TR} can also exist in this semiconductor. The temperature evolution of the hole mobility in CuSCN observed in Figure 7 can therefore be explained by the movement of E_{TR} as described above. We ascribe the transport mechanism of region (1) (see Figure 7) to the MTR model and region (2) to the VRH model. For region (3), the current data appear to be temperature independent, and we are inclined to think that the field-assisted hopping

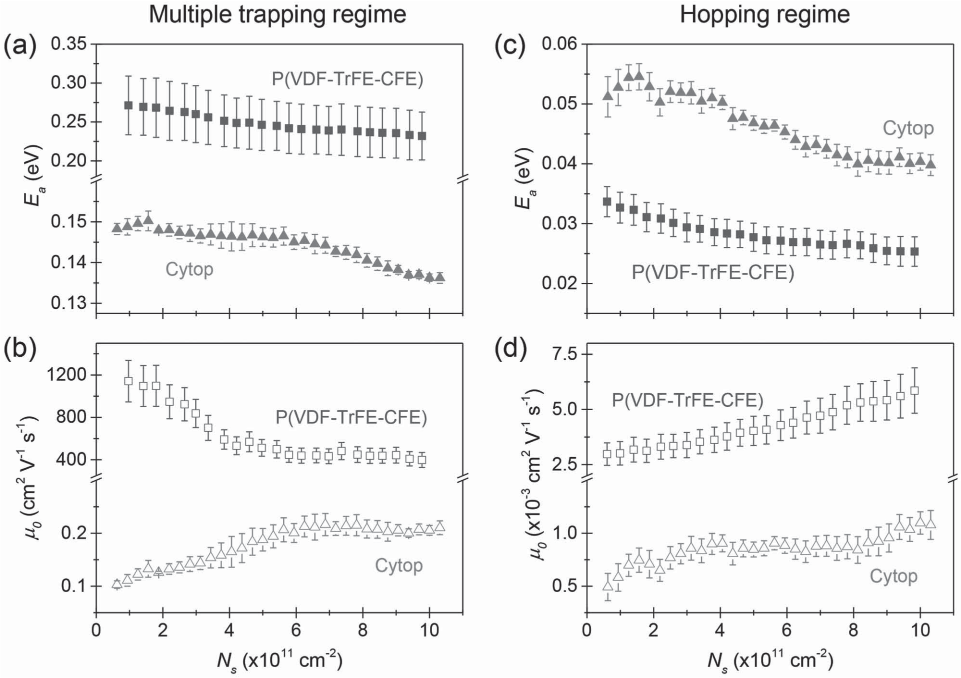

Figure 8. Fitting parameters of the thermally activated mobility [Equation (13)], activation energy (solid symbols) and mobility prefactor (open symbols), for a,b) the MTR and c,d) the VRH transport regimes plotted against gate-induced carrier density for both P(VDF-TrFE-CFE)-based and CYTOP-based CuSCN field-effect transistors.

mechanism is dominant although we acknowledge that more data at even lower temperatures are required in order to draw a conclusive explanation. A study on the electric field dependence would also yield a more complete picture of the carrier transport in all regimes. At this stage, the temperature dependence of μ_{lin} is fitted to the general expression of Equation (13). Choosing a particular transport model would require further work to determine other properties of CuSCN, such as the wavefunction localization length, accurate Fermi energy level, and the nature of phonon interactions, all of which affect the fine details of the transport problem, and hence the specific model. The resulting fitting parameters of Equation (13), i.e., E_a and μ_0, are plotted in **Figure 8** for both the MTR and VRH regimes. It can be seen that E_a of both regimes monotonically decreases with the increasing N_G (which is proportional to V_G) (Figure 8a,c). This is due to the filling of states at energies closer to the mobility edge by the gate field-induced charges, hence decreasing the activation energy.[56] For the VRH regime, E_a of both P(VDF-TrFE-CFE)-based and CYTOP-based transistors are on the order of the characteristic energy E_t (42.4 meV), which supports the theory of E_{TR} as discussed above. On the other hand, for the MTR regime, E_a of P(VDF-TrFE-CFE)-based transistors is significantly larger than that of the CYTOP-based devices. As the MTR regime also covers T_g of P(VDF-TrFE-CFE) which is around 258 K, we presume that the thermal activation of the glass transition adds to E_a in this case.[36] It is also noteworthy that the peak of the mobility of P(VDF-TrFE-CFE)-based devices coincides with the T_g of the dielectric, indicating an interesting relationship between the surface viscoelasticity of the dielectric layer and the electronic properties of the CuSCN. On the other hand, μ_0 [except in the case of MTR transport in P(VDF-TrFE-CFE)-based devices] increases with increasing N_G. As mentioned previously, the exact expression of the mobility prefactor can be complex; for example, Servati et al.[53] have suggested that μ_{FE} also includes, in addition to the physical mobility and the temperature activation, other parameters that depend on the characteristics of the localized states distribution, temperature (weaker dependence compared to the activation term), and carrier concentration. The increase in μ_0 appears to be in agreement with the expression of μ_{FE} derived by these authors, which reflects a result of the inherent dependence on carrier concentration of the definition of μ_{FE}. For the specific case of P(VDF-TrFE-CFE)-based transistors operating in the MTR transport regime which shows a contrasting behavior, we believe that this is also due to the glass transition of the dielectric.

We also note here that the majority of the carrier transport theories involving an exponential DOS of the localized states do not consider the temperature dependence of the DOS itself. Although such behavior discussed in this work still requires further verification, there have also been numerous reports that suggest a correlation between the width of the localized states distribution and the temperature.[45,46] Since the characteristics of the localized states DOS strongly affect the transport properties in noncrystalline semiconductors, we believe that including such phenomena into the transport theory could improve its effectiveness of explaining and predicting the experimental results further.

Finally, we turn our attention to the only major difference between the two sets of transistors—that the average hole mobility of CYTOP-based devices is approximately one order of magnitude lower than that of P(VDF-TrFE-CFE)-based devices throughout the whole temperature range of the measurement (when compared under the same value of N_G). As seen in the previous section, the distributions of the localized states in CuSCN are similar in both cases, and the filling rate of energy states within the semiconductor should therefore be similar. One possible reason may be the Fermi level pinning at the semiconductor/dielectric interface as implied from the different accessible range of qV_0 (which quantifies the band-bending) between the two sets of devices as shown previously in Figure 5a. The result of CYTOP-based devices terminates at approximately 0.1 eV below that of P(VDF-TrFE-CFE)-based devices, possibly indicating that the Fermi level is pinned, resulting in a fewer number of mobile carriers that can contribute to the conductivity as well as suggesting the presence of hole traps and/or fixed charges at the semiconductor/dielectric interface that can adversely affect the hole transport. This, however, is only speculative and more studies are needed to clarify the rather significant difference in the field-effect hole mobility and its relation to the nature of the dielectric-semiconductor interface.

4. Conclusion

In summary, we have studied the hole-transport properties of solution-processed layers of CuSCN using a range of experimental techniques. Capacitance–voltage measurements performed on MIS structures allowed the calculation of the quasistatic semiconductor permittivity $\varepsilon_s = 5.1$ (±1.0), the flat-band voltage $V_{FB} = -0.7$ (±0.1) V, and the unintentional hole doping concentration $N_A = 7.2$ (±1.4) $\times 10^{17}$ cm^{-3}. We ascribe the latter to the acceptor-like states, which could be the result of the presence of unintentional structural defects and/or chemical impurities (presence of solvent molecules etc.). By analyzing the subthreshold characteristics of CuSCN transistors, we have derived the tail states DOS which could be approximated with an exponential function described with a characteristic energy $E_t = 42.4$ (±0.1) meV or an equivalent characteristic temperature $T_t = 492$ (±2) K. A temperature dependence characteristic of the DOS was also observed, exhibiting a decreasing E_t with the decreasing T. The hole-transport process was further studied by analyzing the field-effect hole mobility as a function of temperature from which three transport regimes have been identified. The multiple trapping and release model is found to be able to describe hole transport at higher temperatures (303–228 K) while a variable range hopping process in an exponential DOS becomes dominant at intermediate temperatures (228–123 K). In the lower temperature regime (123–78 K), obtained results suggest the dominance of a field-assisted hopping mechanism although further analysis involving measurements at even lower temperatures would be required. The tremendous potential of CuSCN as a wide bandgap p-type semiconductor in transparent microelectronics as well as a replacement for the commonly used hole-transporting/extracting polymer poly(3,4-ethylenedioxythiophene):polystyrenesulfonate [(PEDOT:PSS)] in OLEDs and OPVs, makes this work timely and provides the foundations for further studies and technological developments.

Acknowledgements

P.P. and T.D.A. are grateful to Cambridge Display Technology (CDT) and Anandamahidol Foundation, Thailand, for financial support.

Received: July 16, 2015
Revised: August 30, 2015

---

[1] P. Pattanasattayavong, G. O. N. Ndjawa, K. Zhao, K. W. Chou, N. Yaacobi-Gross, B. C. O'Regan, A. Amassian, T. D. Anthopoulos, *Chem. Commun.* **2013**, *49*, 4154.
[2] H. J. Snaith, L. Schmidt-Mende, *Adv. Mater.* **2007**, *19*, 3187.
[3] N. Yaacobi-Gross, N. D. Treat, P. Pattanasattayavong, H. Faber, A. K. Perumal, N. Stingelin, D. D. C. Bradley, P. N. Stavrinou, M. Heeney, T. D. Anthopoulos, *Adv. Energy Mater.* **2015**, *5*, 1401529.
[4] N. D. Treat, N. Yaacobi-Gross, H. Faber, A. K. Perumal, D. D. C. Bradley, N. Stingelin, T. D. Anthopoulos, *Appl. Phys. Lett.* **2015**, *107*, 013301.
[5] A. Perumal, H. Faber, N. Yaacobi-Gross, P. Pattanasattayavong, C. Burgess, S. Jha, M. A. McLachlan, P. N. Stavrinou, T. D. Anthopoulos, D. D. C. Bradley, *Adv. Mater.* **2015**, *27*, 93.
[6] G. Heliotis, G. Itskos, R. Murray, M. D. Dawson, I. M. Watson, D. D. C. Bradley, *Adv. Mater.* **2006**, *18*, 334.
[7] S. R. Thomas, P. Pattanasattayavong, T. D. Anthopoulos, *Chem. Soc. Rev.* **2013**, *42*, 6910.
[8] P. Pattanasattayavong, N. Yaacobi-Gross, K. Zhao, G. O. N. Ndjawa, J. Li, F. Yan, B. C. O'Regan, A. Amassian, T. D. Anthopoulos, *Adv. Mater.* **2013**, *25*, 1504.
[9] K. Nomura, H. Ohta, A. Takagi, T. Kamiya, M. Hirano, H. Hosono, *Nature* **2004**, *432*, 488.
[10] E. Fortunato, P. Barquinha, R. Martins, *Adv. Mater.* **2012**, *24*, 2945.
[11] G. R. R. A. Kumara, A. Konno, G. K. R. Senadeera, P. V. V. Jayaweera, D. De Silva, K. Tennakone, *Sol. Energy Mater. Sol. Cells* **2001**, *69*, 195.
[12] S. M. Hatch, J. Briscoe, S. Dunn, *Thin Solid Films* **2013**, *531*, 404.
[13] X. D. Gao, X. M. Li, W. D. Yu, J. J. Qiu, X. Y. Gan, *Thin Solid Films* **2008**, *517*, 554.
[14] B. O'Regan, F. Lenzmann, R. Muis, J. Wienke, *Chem. Mater.* **2002**, *14*, 5023.
[15] B. O'Regan, D. T. Schwartz, *Chem. Mater.* **1995**, *7*, 1349.
[16] L. Ae, J. Chen, M. C. Lux-Steiner, *Nanotechnology* **2008**, *19*.
[17] J. Chen, R. Konenkamp, *Appl. Phys. Lett.* **2003**, *82*, 4782.
[18] S. M. Hatch, J. Briscoe, S. Dunn, *Adv. Mater.* **2013**, *25*, 867.
[19] C. Lévy-Clément, R. Tena-Zaera, M. A. Ryan, A. Katty, G. Hodes, *Adv. Mater.* **2005**, *17*, 1512.
[20] M. Grünewald, P. Thomas, D. Würtz, *Phys. Status Solidi B* **1980**, *100*, K139.
[21] J. Li, D. Liu, Q. Miao, F. Yan, *J. Mater. Chem.* **2012**, *22*, 15998.
[22] J. Li, Z. Sun, F. Yan, *Adv. Mater.* **2012**, *24*, 88.
[23] E. H. Nicollian, J. R. Brews, *MOS (Metal Oxide Semiconductor) Physics and Technology*, John Wiley & Sons, Hoboken, NJ, USA, **1982**.
[24] S. M. Sze, K. K. Ng, *Physics of Semiconductor Devices*, John Wiley & Sons, Hoboken, NJ, USA, **2007**.
[25] W. L. Kalb, B. Batlogg, *Phys. Rev. B* **2010**, *81*, 035327.
[26] I. Hamberg, C. G. Granqvist, *J. Appl. Phys.* **1986**, *60*, R123.
[27] H. Yoshikawa, S. Adachi, *Jpn. J. Appl. Phys.* **1997**, *36*, 6237.
[28] C.-M. Wang, J.-F. Wang, H.-C. Chen, W.-B. Su, G.-Z. Zang, P. Qi, M.-L. Zhao, *Mater. Sci. Eng., B* **2005**, *116*, 54.
[29] S. Tavazzi, A. Borghesi, A. Papagni, P. Spearman, L. Silvestri, A. Yassar, A. Camposeo, M. Polo, D. Pisignano, *Phys. Rev. B* **2007**, *75*, 245416.

[30] C. H. Kim, O. Yaghmazadeh, D. Tondelier, Y. B. Jeong, Y. Bonnassieux, G. Horowitz, *J. Appl. Phys.* **2011**, *109*, 2699.
[31] Y. S. Cho, R. R. Franklin, *Trans. Electr. Electron. Mater.* **2012**, *13*, 237.
[32] M. Kabešová, M. Dunaj-jurčo, M. Serator, J. Gažo, J. Garaj, *Inorg. Chim. Acta* **1976**, *17*, 161.
[33] D. L. Smith, V. I. Saunders, *Acta Crystallogr., Sect. B: Struct. Commun.* **1981**, *37*, 1807.
[34] D. L. Smith, V. I. Saunders, *Acta Crystallogr., Sect. B: Struct. Commun.* **1982**, *38*, 907.
[35] V. Bobnar, B. Vodopivec, A. Levstik, M. Kosec, B. Hilczer, Q. M. Zhang, *Macromolecules* **2003**, *36*, 4436.
[36] H.-M. Bao, J.-F. Song, J. Zhang, Q.-D. Shen, C.-Z. Yang, Q. M. Zhang, *Macromolecules* **2007**, *40*, 2371.
[37] J.-F. Capsal, E. Dantras, C. Lacabanne, *J. Non-Cryst. Solids* **2013**, *363*, 20.
[38] J. E. Jaffe, T. C. Kaspar, T. C. Droubay, T. Varga, M. E. Bowden, G. J. Exarhos, *J. Phys. Chem. C* **2010**, *114*, 9111.
[39] M. Shur, M. Hack, *J. Appl. Phys.* **1984**, *55*, 3831.
[40] P. G. Le Comber, W. E. Spear, *Phys. Rev. Lett.* **1970**, *25*, 509.
[41] P. G. Le Comber, A. Madan, W. E. Spear, *J. Non-Cryst. Solids* **1972**, *11*, 219.
[42] A. Troisi, G. Orlandi, *Phys. Rev. Lett.* **2006**, *96*, 086601.
[43] A. Troisi, G. Orlandi, *J. Phys. Chem. A* **2006**, *110*, 4065.
[44] H. Mueller, P. Thomas, *Phys. Rev. Lett.* **1983**, *51*, 702.
[45] G. D. Cody, T. Tiedje, B. Abeles, B. Brooks, Y. Goldstein, *Phys. Rev. Lett.* **1981**, *47*, 1480.
[46] S. Aljishi, J. D. Cohen, S. Jin, L. Ley, *Phys. Rev. Lett.* **1990**, *64*, 2811.
[47] G. Horowitz, M. E. Hajlaoui, R. Hajlaoui, *J. Appl. Phys.* **2000**, *87*, 4456.
[48] R. A. Street, J. E. Northrup, A. Salleo, *Phys. Rev. B* **2005**, *71*, 165202.
[49] R. Bourguiga, G. Horowitz, F. Garnier, R. Hajlaoui, S. Jemai, H. Bouchriha, *Eur. Phys. J.: Appl. Phys.* **2002**, *19*, 117.
[50] K. Tennakone, W. M. Ariyasingha, *Electrochim. Acta* **1980**, *25*, 731.
[51] S. Lee, A. Nathan, *Appl. Phys. Lett.* **2012**, *101*, 113502.
[52] T. Tiedje, A. Rose, *Solid State Commun.* **1981**, *37*, 49.
[53] P. Servati, A. Nathan, G. A. J. Amaratunga, *Phys. Rev. B* **2006**, *74*, 245210.
[54] D. Monroe, *Phys. Rev. Lett.* **1985**, *54*, 146.
[55] M. Grünewald, B. Movaghar, B. Pohlmann, D. Würtz, *Phys. Rev. B* **1985**, *32*, 8191.
[56] M. C. J. M. Vissenberg, M. Matters, *Phys. Rev. B* **1998**, *57*, 12964.
[57] S. D. Baranovskii, T. Faber, F. Hensel, P. Thomas, *J. Phys.: Condens. Matter* **1997**, *9*, 2699.
[58] H. Fritzsche, *J. Non-Cryst. Solids* **1989**, *114*, 1.
[59] P. Thomas, S. D. Baranovskii, *J. Non-Cryst. Solids* **1993**, *164*, 431.
[60] F. R. Shapiro, D. Adler, *J. Non-Cryst. Solids* **1985**, *74*, 189.
[61] E. A. Davis, N. F. Mott, *Philos. Mag.* **1970**, *22*, 0903.
[62] V. N. Prigodin, A. J. Epstein, *Phys. Rev. Lett.* **2007**, *98*, 259703.
[63] J. H. Worne, J. E. Anthony, D. Natelson, *Appl. Phys. Lett.* **2010**, *96*, 053308.
[64] D. Bourbie, *Appl. Phys. Lett.* **2011**, *98*, 012104.
[65] M. H. Cohen, E. N. Economou, C. M. Soukoulis, *J. Non-Cryst. Solids* **1984**, *66*, 285.
[66] J. Orenstein, M. Kastner, *Phys. Rev. Lett.* **1981**, *46*, 1421.
[67] E. A. Schiff, *J. Phys.: Condens. Matter* **2004**, *16*, S5265.